Thin Solid Films 562 (2014) 211–217

Contents lists available at ScienceDirect

Thin Solid Films

journal homepage: www.elsevier.com/locate/tsf

Synthesis of sub-10-nm Sn nanoparticles from Sn(II) 2-ethylhexanoate by a modified polyol process and preparation of Ag – Sn film by melting of the Sn nanoparticles

Sang-Soo Chee, Jong-Hyun Lee *

Department of Materials Science and Engineering, Seoul National University of Science and Technology, Seoul 139-743, Republic of Korea

ARTICLE INFO

Article history:
Received 16 July 2013
Received in revised form 14 April 2014
Accepted 15 April 2014
Available online 24 April 2014

Keywords:
Tin
Silver
Nanoparticles
Modified polyol synthesis
Sn(II) 2-ethylhexanoate
Melting point
Composite ink

ABSTRACT

Ultrafine Sn nanoparticles (NPs) (diameter < 10 nm) exhibiting a remarkable depression in their melting point were synthesized at room temperature by a modified polyol process. For the synthesis, low-grade Sn(II) 2-ethylhexanoate and sodium borohydride were used as the precursor and reducing agent in a diethylene glycol medium. Further, polyvinyl pyrrolidone was used as a capping agent during the synthesis. The synthesized crystalline Sn NPs showed an average diameter of 7.98 nm and an extremely low melting point of 128 °C. To test the applicability of the synthesized ultrafine Sn NPs to practical systems, an Ag-based composite ink containing the Sn NPs was prepared. The ink was easily sintered through local liquid-phase sintering by melting of the ultrafine Sn NPs added as a metal binder. Therefore, despite the low-temperature (170 °C) sintering with a short duration (~15 min), the composite ink exhibited excellent sheet resistance.

1. Introduction

Sn is the main element in solder alloys that are the most widely used interconnection materials in the electronics packaging industry. Binary or ternary Sn-based alloys are preferred over pure Sn as solder materials owing to various reasons. The most important reason, however, is that the use of these alloys decreases the required interconnection temperature because of their low melting points. Nevertheless, some typical Pb-free solder alloys have high melting points, e.g., Sn–3.0Ag–0.5Cu (wt.%) (melting point: 217 °C). The use of high-melting-point Pb-free solder alloys is detrimental to the thermal stability of polymer materials with a low glass transition temperature (T_g) that are widely used in the electronics packaging industry. Furthermore, a high processing temperature may induce cumulative stress at interfaces between packaging materials with different values of the coefficient of thermal expansion; this stress may result in the warpage of packages or delamination at the interfaces [1–3]. In addition, soldering at high temperatures is uneconomical because of high energy consumption.

However, the use of solder alloys with disproportionately low melting points may also be problematic, as recently observed in the case of mobile electronics in which excessive heat emission made low-melting-point solder joints unreliable [4–6]. Further, Sn–58Bi alloy—a typical low-melting-point alloy—has been reported to be extremely brittle when subjected to rapid stress loading [7–11]. Hence, alternative solder materials with bimodal melting behavior—exhibiting low melting points during reflow soldering and high melting points after it—are highly desirable.

The melting point of metal particles tends to decrease considerably when the particle size is reduced to less than a few tens of nanometers [12]. This phenomenon of melting point depression due to reduction in the particles is known as the Gibbs–Thomson effect. Therefore, Sn nanoparticles (NPs) with sizes less than a few tens of nanometers would show a considerable reduction in the melting point, and this reduction may enable the formation of interconnections at extremely low temperatures. Jo et al. synthesized fine Sn NPs with average diameters in the range 11.3–29.1 nm by a modified polyol process [13]. They found the melting point of the Sn NPs with an average diameter of 11.3 nm to be 177.3 °C. Moreover, they demonstrated experimentally that the lesser the particle size the more the reduction in the melting point. Huang and Duh reported the fabrication of Sn NPs smaller than those reported by Jo et al. [14]. They adopted a reduction-based synthesis process that involved mixing a Sn chloride precursor with excess reductant in a reaction bath, and reported the formation of uniformly fine Sn NPs with an average diameter of 10.4 nm [14]. However, they did not measure the melting points of the synthesized NPs. In summary, the tendency of the melting point of pure Sn to decrease markedly with a decrease in the particle size may be utilized to eliminate the necessity for the preparation of ternary Sn-based solder alloys, which is performed for reducing the

* Corresponding author at: Department of Materials Science and Engineering, Seoul National University of Science and Technology, 232 Gongneung-ro, Nowon-gu, Seoul 139-743, Republic of Korea. Tel.: +82 2 970 6612; fax: +82 2 973 6657.
E-mail address: pljh@snut.ac.kr (J.-H. Lee).

http://dx.doi.org/10.1016/j.tsf.2014.04.061
0040-6090/

processing temperature. Moreover, Sn NPs coagulate or agglomerate with each other during reflow soldering or sintering and growth, resulting in the formation of bulk Sn, which has a melting point of 232 °C [13]. Thus, the drawback of low-melting-point solder alloys adversely affecting thermal stability may be prevented. Moreover, fine Sn NPs when converted into a solder paste or an ink may be used in fine pitch interconnections, which are one of the immediate requirements of the electronics industry [13,15]. Although binary or ternary Sn-based alloy NPs have the advantage of lower melting point, the synthesis of these alloy NPs via chemical reduction takes a long time and it is difficult to uniformly and precisely control the alloy composition [16–18].

Current research on the application of Sn NPs is mostly focused on preparing conductive inks for inkjet printing, although the electrical conductivity of Sn is inherently lower than that of Ag or Cu [13]. In the present study, however, Sn NPs were used as a metal binder that melts at extremely low temperatures. A significant melting point reduction of >100 °C can be achieved by synthesizing ultrafine Sn NPs with diameters <10 nm [13,19,20]. Thus, the addition of ultrafine Sn NPs to commercial Ag inks can reduce the thermal sintering temperature, which is as high as 200–300 °C, and holding time required to obtain good conducting tracks owing to the melting of Sn NPs. The distinct sintering temperature reduction is extraordinarily significant for industrial applications, considering the low cost of polymer films that exhibit a low T_g.

2. Experimental details

In the present study, ultrafine Sn NPs were synthesized by a modified polyol process. The process involved the decomposition of a metal precursor and reduction of the metal ions in a polyol medium. Sn(II) 2-ethylhexanoate ($[CH_3(CH_2)_3CH(C_2H_5)CO_2]_2Sn$, ~95%) and sodium borohydride ($NaBH_4$, 99.99%) were used as the metal precursor and reducing agent, respectively. In this process, polyvinyl pyrrolidone (PVP, molecular weight: 1,300,000, Aldrich Chemical Co.), a capping agent, was also used to suppress agglomeration between the synthesized NPs and to prevent their excessive oxidation [13,18]. All chemicals except PVP were supplied by Sigma-Aldrich Co. and used as-received without further processing or purification. Sn(II) 2-ethylhexanoate used in this study had the highest commercially available purity.

Sn NPs were synthesized in air at room temperature by injecting Sn(II) 2-ethylhexanoate into the diethylene glycol (DEG) solution containing sodium borohydride and PVP. To prepare the solution, 2 g of sodium borohydride and 1 g of PVP were dissolved completely in 100 ml of DEG. Then, 2 ml of Sn(II) 2-ethylhexanoate was directly injected into this solution by using a dispenser at the rate of ~4.5 ml/min. This procedure was different from the modified polyol process employed by Jo et al. They used Sn(II) acetate and 1,5-pentanediol as the precursor and polyol medium, respectively, and injected the reductant solution into the Sn precursor solution in an argon atmosphere at >100 °C [13].

After adding the starting materials to the DEG solution, the obtained final solution was continuously stirred using a magnetic pellet for 60 min to provide sufficient time for reaction completion. Samples for high-resolution transmission electron microscopy (HRTEM, Tecnai G^2 F30ST, FEI Company), carried out at 300 kV to elucidate the morphology, size distribution, and crystal structure of the synthesized Sn NPs, were prepared by adding a few drops of the final DEG solution on to Cu grids coated with a carbon film.

To estimate the reduction in their melting point, thermal analysis of the Sn NPs was carried out by differential scanning calorimetry (DSC, Q20, TA Instruments). To allow free evaporation of DEG, the pan lid was removed during the DSC experiments. The initial mass of the sample was ~10 mg and it was heated from 30 °C to 250 °C at the rate of 10 °C/min. To prevent oxidation during heating, the experiments were carried out under a nitrogen flow (50 ml/min). For comparison, DSC measurements on dried Sn NPs were also performed under identical experimental conditions.

The dried Sn NPs were prepared via an additional drying step carried out in a vacuum chamber maintained at room temperature. Because DEG takes a long time to dry owing to its low volatility, additional medium-exchanging steps were carried out in which DEG was repetitively exchanged with methanol using a centrifuge. The centrifugation was performed for 30 min at 6000 rpm during each medium-exchanging step and the solution was condensed in the last cycle.

The dried NPs were also subjected to X-ray photoelectron spectroscopy (XPS, K-Alpha, Thermo Electron Co.) using the monochromated Al Kα X-ray (1486.6 eV). Beam energy was set at 12 kV and current density was at 6 mA. Additionally, Fourier transform infrared (FT-IR, Vertex 80, Bruker Optics Co.) analysis was performed, and X-ray diffraction (XRD, X'pert PRO-MPD, PANalytical) analysis was also carried out in the 2θ range 20–90° using Cu-Kα radiation. During the preparation of the powder samples for XRD analysis, the centrifuge speed was increased to 15,000 rpm to gather more NPs. In addition, inductively coupled plasma atomic emission spectroscopy (ICP-AES, JY Ultima2C, Jobin Yvon Inc.) was performed to investigate the composition of the dried NPs.

Further, a small amount of the Sn NPs dispersed in methanol was added to a commercial Ag ink (DGP 40TE-20C, Advanced Nano Products Co., average diameter of Ag NPs: 42.8 nm) to fabricate a Ag/Sn composite ink; it was anticipated that this ink would exhibit local low-temperature melting and sintering characteristics. The ultrafine Sn NPs added to the composite ink were expected to perform as metal binders that could melt at low temperatures. The PVP capping in the Sn NPs has been reported to deter the achievement of stable electrical conductivity [13]. Hence, before their addition to the ink, the Sn NPs were subjected to an additional washing step that involved a centrifugation step in an acetone/methanol solution, a medium-exchanging step, and a condensing step.

A small amount of the composite ink (70 μl) was dropped onto a Si wafer (1 cm × 1 cm) using a micropipette (Research Plus 3120 000.046, Eppendorf). The Si wafer coated with the composite ink was sintered in an air atmosphere for 15 min at 170 °C. The microstructure of the sintered layer was then analyzed by field-emission scanning electron microscopy (FE-SEM, Hitachi S-4200, Hitachi Ltd.), and its composition was obtained by energy-dispersive X-ray spectroscopy (EDS, Horiba EMAX 6853-H, Horiba Ltd.). A surface topography for the sintered film was measured using an atomic force microscope (AFM, Nanoscope IV, Digital Instruments). Further, the sheet resistance of the sintered layer was measured using a four-point prober linked to a source meter (2400, Keithley Instruments Inc.). The total distance between the probes set at an interval of 1 mm was 3 mm and a correction factor of 4.22 was used in the calculation of sheet resistance, taking into account the sample size and thickness.

3. Results and discussion

Fig. 1(a) shows the TEM images of the as-synthesized Sn NPs. The NPs were discrete (without agglomeration) and exhibited spherical or ovoid (i.e., slightly elongated and spherical) morphologies. Although the diameters of the NPs were observed to range from 4 to 13 nm, most of the particles had diameters between 5 nm and 10 nm, indicating a narrow size distribution (Fig. 1(b)). The average diameter of the NPs was found to be 7.98 nm (standard deviation: <20%). The HRTEM image shown in Fig. 1(c) indicates the presence of crystalline structures and the selected area electron diffraction (SAED) pattern in Fig. 1(d) confirmed the presence of β-Sn. The clear ring fringes indicated that crystallization occurred along different growth planes in a group of NPs or in an individual NP. The interplanar distance was measured to be 0.29 nm, as shown in the inset of Fig. 1(d), which corresponds to the interplanar distance between the (200) planes of β-Sn. The narrow size distribution of the NPs, in contrast to that observed in an earlier study performed without the addition of PVP [21], indicated indirectly that the surfaces of the NPs synthesized in this study were surrounded by PVP.

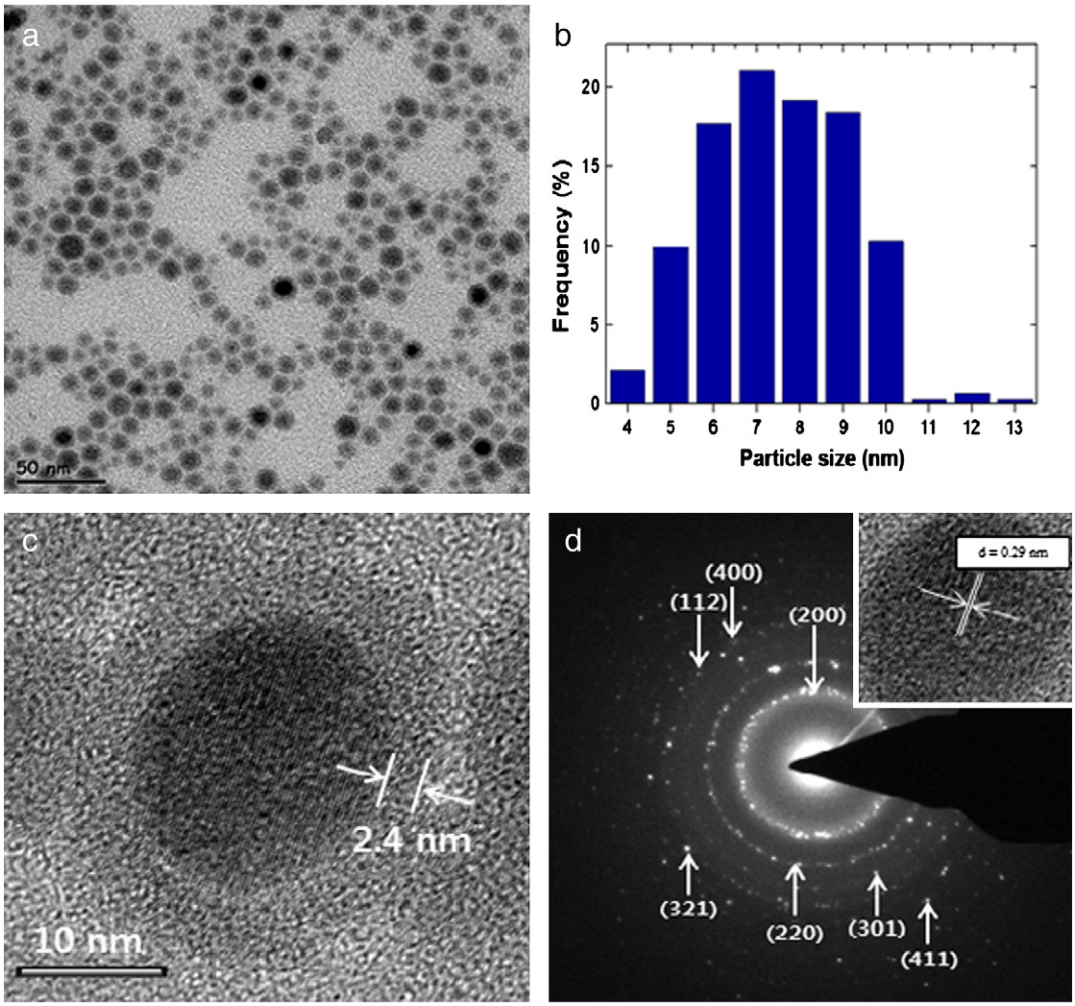

Fig. 1. TEM images of Sn NPs synthesized by the modified polyol process: (a) low-magnification image, (b) particle size (diameter) distribution, (c) high-magnification image, and (d) SAED pattern and high-resolution TEM image (inset).

The reduction of Sn ions supplied by the precursor could be represented by the reaction given below [16]:

$$BH_4^- + 8OH^- + 4Sn^{2+} \rightarrow B(OH)_4^- + 4H_2O(g) + 4Sn. \quad (1)$$

Reaction (1) can be further divided into a pair of redox reactions, as shown below:

$$BH_4^- + 8OH^- \rightarrow B(OH)_4^- + 4H_2O + 8e^- \quad (2)$$

$$4Sn^{2+} + 8e^- \rightarrow 4Sn. \quad (3)$$

While reaction (2) occurred in the DEG solution containing sodium borohydride, reduction reaction (3) occurred when the Sn(II) 2-ethylhexanoate solution was injected into the solution of sodium borohydride and PVP in DEG. Before reaction (3), a coordination bond may have been formed between the Sn ions and lone-pair electrons of the oxygen atom on the carbonyl group of PVP [13]. Subsequently, the reduced Sn atoms were consumed for the nucleation and growth of the Sn NPs. During the synthesis of Sn NPs, the chemical bonding of PVP suppressed the oxidation of Sn ions and the agglomeration between the as-synthesized Sn NPs.

The Sn NPs synthesized in this study showed sizes (4–13 mm) smaller than those reported in a previous study (11.3–29.1 nm). This "fine-tuning" of the size of the synthesized Sn NPs is believed to be mainly caused by three reasons. Firstly, the low temperature process employed in this study is considered to be one of the reasons. The size of Sn NPs synthesized by the modified polyol route increases with an increase in the synthesis temperature, which is in contrast with the classical polyol process [13,22,23]. In this study, the modified polyol process was carried out at room temperature. The Sn atoms, easily reduced even at room temperature by the addition of a strong reductant (sodium borohydride), formed nuclei and these nuclei then grew. During the growth, however, a high temperature may induce greater collision coagulation between NPs synthesized in the medium. Secondly, the low grade of the starting material (Sn(II) 2-ethylhexanoate) might have been effective in the synthesis of ultrafine Sn NPs. Impurity ions present in the medium, coming from the low-purity precursor, might have disrupted the reduction reaction (3) and reduced the number of Sn atoms per unit volume [24]. The resulting low atom density might have restricted the initial size of Sn nuclei. Finally, it was predicted that the characteristic size and size distribution of the NPs obtained by the modified polyol process were dependent on the polyol type [25]. The reduction kinetics of Sn ions in the modified polyol process employed in this study may vary depending on the transferability of electrons supplied by reaction (2) as a function of the polyol type. If the reduction rate is high enough, the concentration of reduced Sn atoms will increase rapidly and become greater than the saturation concentration until nucleation occurs, as explained by La Mer [26,27]. The short burst in nucleation due to the rapid increase in Sn concentration results in the formation of a large number of nuclei [28]. These nuclei grow rapidly and the Sn

concentration drops to a point below the nucleation concentration but high enough to allow small particle growth to occur at a rate that just consumes all the generated Sn [23,29]. In summary, the polyol type might have affected the reduction rate; the short burst in nucleation might have generated fine particles, resulting in a narrow size distribution.

Fig. 2 shows the XPS analysis results for dried Sn NPs. The spectrum indicates two main peaks corresponding to the spin-orbital coupling of the 3d state with a spin–orbit separation of 8.4 eV. The peak assigned to Sn $3d_{5/2}$ can also be separated into two peaks [30]. One peak at 484.5 eV originated from Sn [31]. However, the other peak at 486.7 eV was found to originate from SnO_x, implying that oxides were formed on the surface of the Sn NPs during the synthesis or drying [32,33].

Although an oxide-like layer was observed on the Sn NPs, as shown in Fig. 1(c), the layer did not give rise to a specific diffraction pattern. Therefore, it is inferred that the surfaces of the synthesized Sn NPs were surrounded by SnO_x and PVP molecules, forming a previously reported oxide–organic complex layer [13,18,28]. While the thickness of this complex layer was irregular, the measured maximum thickness did not exceed ~3.7 nm.

The formation of an oxide–organic complex layer can be elucidated more reliably on the basis of FT-IR analysis results, shown in Fig. 3. In the spectra for pure PVP and synthesized Sn NPs, the peaks at 3016–2815, 1753–1519, 1517–1346, and 1344–1110 cm^{-1} correspond to the C – H stretching [34], C═O stretching [34–36], – CH_2 bending [34,37], and C – N stretching vibrations [34,37], respectively. The peak at 3648–3085 cm^{-1} was confirmed to originate from the moisture absorbed in the PVP [34,37]. In addition, the peak observed at 767–638 cm^{-1} corresponds to the Sn – O group [38], which correlated well with the XPS analysis results. Consequently, the FT-IR spectra indicated that PVP and the oxide adhered to the surface of the synthesized Sn NPs [39]. The negative shift and broadening of the peaks corresponding to the C═O and C – N stretching vibrations and the – CH_2 bending vibration were attributed to the formation of small NPs and chemical bonding, respectively [35–37].

The XRD patterns for the dried Sn NPs are shown in Fig. 4. While the diffraction peaks were broadened because the powders were nanosized, many peaks, including the main peak corresponding to (200) reflections, can be clearly observed. Despite the formation of an oxide–organic complex layer, no discrete peaks corresponding to SnO_x can be observed, confirming that the oxide formation was insignificant, leading to a thin surface layer. The average size of the Sn NPs was estimated from the average full width at half maximum of the (200) peak, according to Scherrer's equation. The value obtained was ~22 nm, which is larger than that obtained from Fig. 1(a). This can be attributed to the particle growth due to the coalescence of the synthesized Sn NPs during the high-speed centrifugation at 15,000 rpm [22,40].

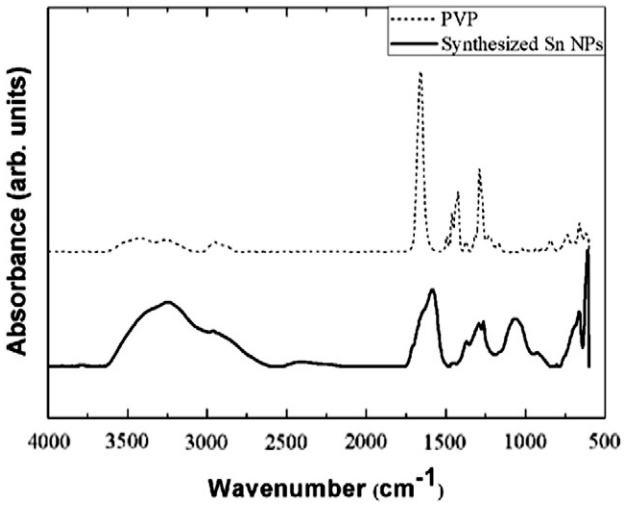

Fig. 3. FT-IR spectra for pure PVP and Sn NPs synthesized in DEG containing PVP.

The elemental composition of the dried Sn NPs measured using ICP-AES is summarized in Table 1. Even though the purity of the starting material was quite low (~95%), the purity of the synthesized Sn NPs approached 99.8 wt.%, indicating the advantage of the modified polyol process. Therefore, ultrafine high-purity Sn NPs can be obtained by the modified polyol process employed in the present study.

Fig. 5 shows the DSC analysis results for DEG containing the as-synthesized Sn NPs and dried Sn NPs. A sample of the DEG solution containing the NPs showed no distinct peaks except for a peak corresponding to the evaporation of DEG during the first heating cycle. This is because the concentration of the Sn NPs in the solution was insufficient to be clearly measured. However, a relatively sharp endothermic peak was detected at 128 °C during the second heating cycle performed after DEG was sufficiently removed during first heating. This indicates the representative melting of the remaining Sn NPs, shown by the remarkable reduction in the melting point at 104 °C in comparison to that for bulk Sn. This is one of the lowest reported values in the literature. Lai et al. proposed Eq. (4) for estimating the size dependence of the melting point of Sn NPs on the basis of Hanszen model [19]. In this model, it is assumed that a solid particle is embedded in a thin liquid overlayer, and the melting temperature is taken to be the temperature

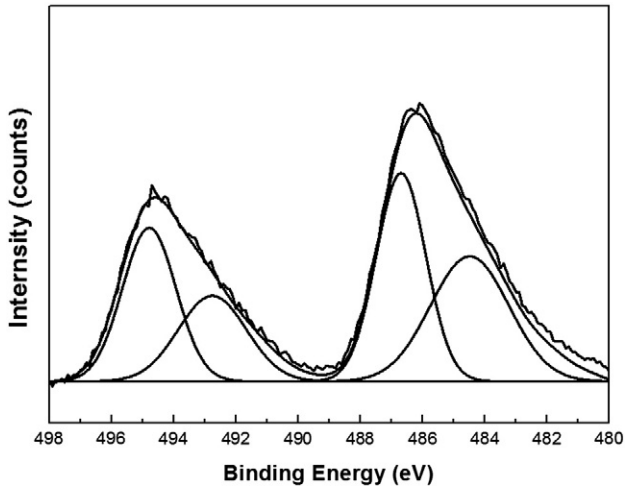

Fig. 2. XPS spectra for as-prepared Sn NPs.

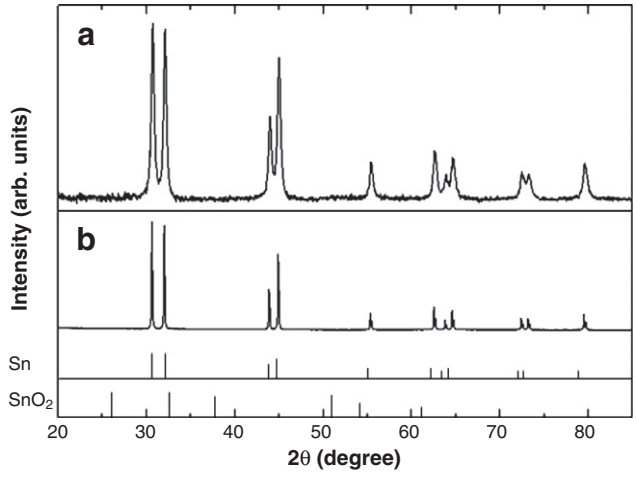

Fig. 4. XRD patterns for (a) as-prepared Sn NPs and (b) sub-micron Sn powders.
S.-S. Chee et al., Res. Chem. Intermed., in press.

Table 1
Elemental composition of as-prepared Sn NPs measured by ICP-AES.

Element	Concentration (ppm)	Concentration (at.%)
Sn	Balance	99.774
Co	<3	–
Cr	7.395	0.001
Cu	64.59	0.006
Fe	1733	0.173
Ni	<3	–
Pb	269.7	0.027
Zn	187.3	0.019
Sb	<3	–

of equilibrium between the solid sphere core and the liquid overlayer with a given critical thickness (t_0).

$$T_m = 232 - 782\left[\frac{\sigma_{sl}}{15.8(r - t_0)} - \frac{1}{r}\right] \quad (4)$$

where T_m (°C) is the melting point of a particle with a radius r (Å), and σ_{sl} is the interfacial surface tension between the solid and liquid. From their experimental data, Lai et al. determined σ_{sl} to be 48 ± 8 mN/m, and the best fit for t_0 to be 18 Å.

The average radius of the Sn NPs shown in Fig. 1(a) was ~4.0 nm; using this value in Eq. (4) for an σ_{sl} value of 55 mN/m, the melting point is obtained to be 128 °C. This value is consistent with the melting point observed in the second cycle of Fig. 5(a). Meanwhile, the sample prepared with completely dried Sn NPs revealed a sharp peak at ~140 °C during the first heating cycle. This indicates the melting point of the dried Sn NPs, which corresponds to a reduction of 92 °C in the melting point. This slight increase in the melting point when compared to that shown in Fig. 5(a) is attributed to the coagulation or agglomeration of the NPs during centrifugation and drying [22,40]. In Eq. (4), the increase corresponds to an increase of ~0.27 nm in the radius of the NPs; this difference is too small to detect from a micrograph.

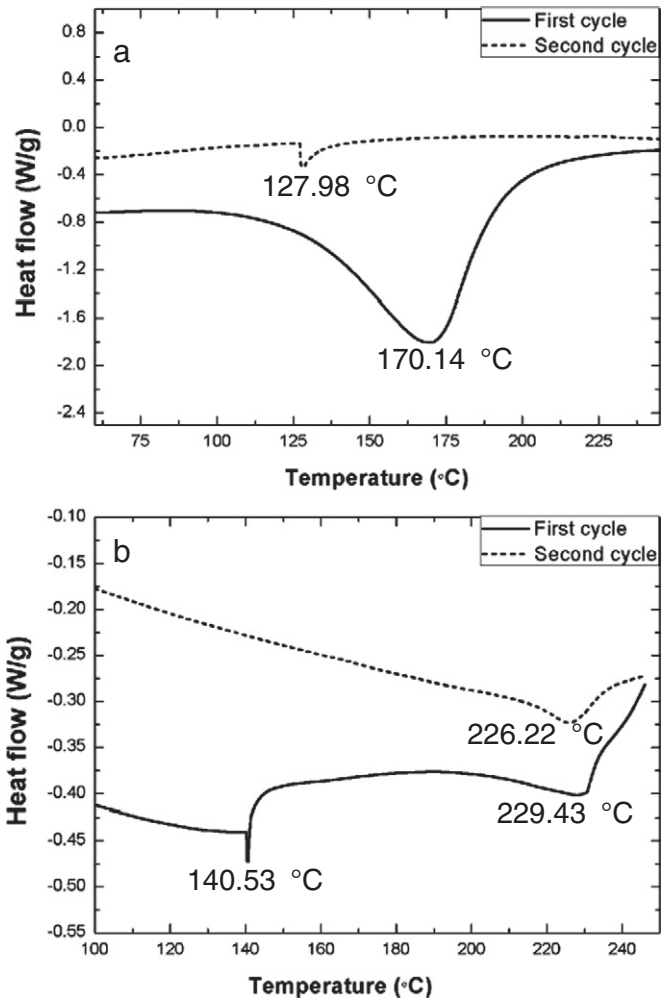

Fig. 5. DSC curves for (a) as-synthesized Sn NPs dispersed in DEG and (b) dried Sn NPs.

Further, a slightly broad peak was detected at 230 °C during the first heating cycle, which is indicative of the remelting (near the bulk Sn melting point) of coarse Sn NPs that were agglomerated by melting at ~140 °C [13]. It should be noted here that NPs with a diameter >30 nm were not observed in Fig. 1(a). The Sn agglomerates melted only at temperatures close to the melting point of bulk Sn during subsequent repetitive heating cycles (including the second heating cycle), indicating that the melting point reduction characteristics were absent in the agglomerates.

The results in Fig. 5 also present the relationship between the PVP capping thickness and the agglomeration. In the dried Sn NPs thinly capped with PVP by the repetitive washing with methanol, another endothermic peak (the remelting of agglomerated Sn NPs) was observed at 230 °C during the first heating cycle (Fig. 5b). However, the as-synthesized Sn NPs which were thickly capped with PVP did not indicate the formation of another endothermic peak at any point close to the melting point of bulk Sn during the second heating cycle (Fig. 5a), implying that the agglomeration process between the Sn NPs did not occur.

The Ag/Sn composite ink containing the Sn NPs synthesized in this study was sintered to verify the feasibility of ultrafine Sn NPs acting as a liquid metal binder to achieve lower processing temperatures and shorter holding times during the sintering of commercial Ag ink. The sintering temperature of the Ag/Sn composite ink was higher than the representative melting point of the synthesized Sn NPs by ~40 °C, resulting in sufficient wettability for the molten NPs. As a result, the sheet resistance of the Ag–3.14Sn (vol.%) layer sintered for 15 min at 170 °C (2.29×10^{-3} Ω/sq.) was slightly lower than that of the pure Ag layer (2.54×10^{-3} Ω/sq.) sintered for 60 min at 220 °C.

Fig. 6 shows the surface microstructures of the pure Ag layer sintered for 60 min at 220 °C and the Ag–3.14Sn layer sintered for 15 min at 170 °C. The average size of the particles observed in the Ag layer was larger than that of the particles in the Ag–3.14Sn layer, indicating accelerated solid-state sintering of the Ag particles at high sintering temperatures. However, the connectivity between the particles was better in the Ag–3.14Sn layer and a clearly agglomerated microstructure was frequently observed for the sample. Fig. 7 shows the surface topography of a Ag–3.14Sn (vol.%) layer sintered for 15 min at 170 °C. On the whole, there were elongated half-oval patterns throughout the surface with coalescence of Ag and Sn NPs. Fine protuberances equivalent to the sizes of Ag NPs were also observed. The mean roughness R_a from the surface profile was 4.40 nm. The microstructure was formed through local liquid-phase sintering due to melting of the ultrafine Sn NPs added to function as metal binders. The ultrafine Sn NPs, which melted at a temperature (170 °C) higher than the melting point of the NPs, were expected to wet the Ag particles circumferentially, resulting in highly connected Ag particles and agglomerated microstructures. Consequently, the enhanced sheet resistance of the Ag–3.14Sn composite ink was attributed to the enhanced connectivity. This confirms the excellent quality of the synthesized Sn NPs and the feasibility for their use as a liquid metal binder. If the melted Sn NPs can wet the surface of the Ag particles, the melted Sn may solidify instantly owing to the rapid increase in the radius of curvature. Hence, the role of the added Sn NPs as a binder is thought to be temporary, and the connection mechanism between the Ag particles can be expressed in transient liquid phase sintering. For this reason, sintering at slightly higher temperatures or with longer holding times did not rapidly lower the sheet resistance of the Ag – Sn composite layers.

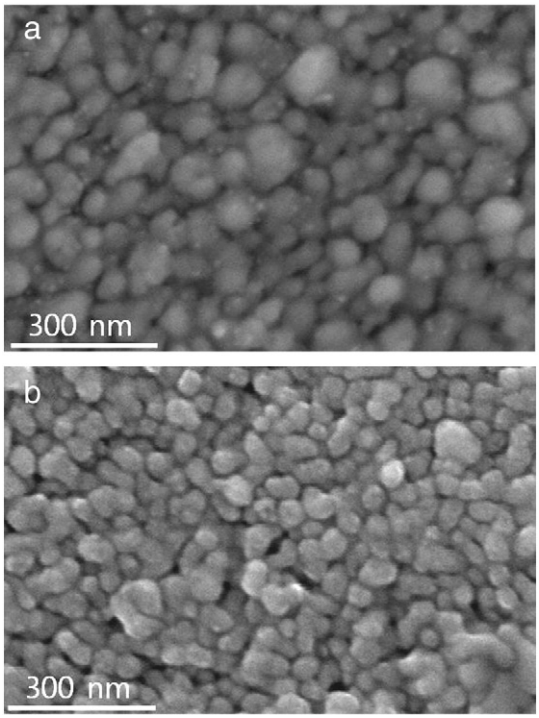

Fig. 6. SEM images of the surface of (a) a pure Ag layer sintered for 60 min at 220 °C, and (b) a Ag–3.14Sn (vol.%) layer sintered for 15 min at 170 °C.

4. Conclusions

Ultrafine Sn particles were synthesized at room temperature by a modified polyol process, using low-grade Sn(II) 2-ethylhexanoate as the precursor. The diameter of the synthesized Sn NPs, which exhibited crystalline structures, ranged from 4 to 12 nm with an average value of 7.98 nm. Characterization of the synthesized Sn NPs by HRTEM, XPS, and FT-IR analyses indicated the formation of an oxide–organic complex layer on the NPs. However, the XRD analysis results and wetting behavior of the Sn NPs on larger Ag NPs revealed that the oxidation was not significant. The purity of the Sn precursor was only ~95%, but that of the synthesized Sn NPs approached 99.8%. In addition, the synthesized Sn NPs exhibited an extremely low melting point of 128 °C, which is remarkably lower than that of bulk Sn by 104 °C. In a preliminary attempt to find applications for the synthesized Sn NPs, a Ag-based composite ink containing the synthesized Sn NPs was prepared. This composite ink showed excellent sheet resistance even under mild sintering conditions of a low temperature (170 °C) and a short treatment time (15 min).

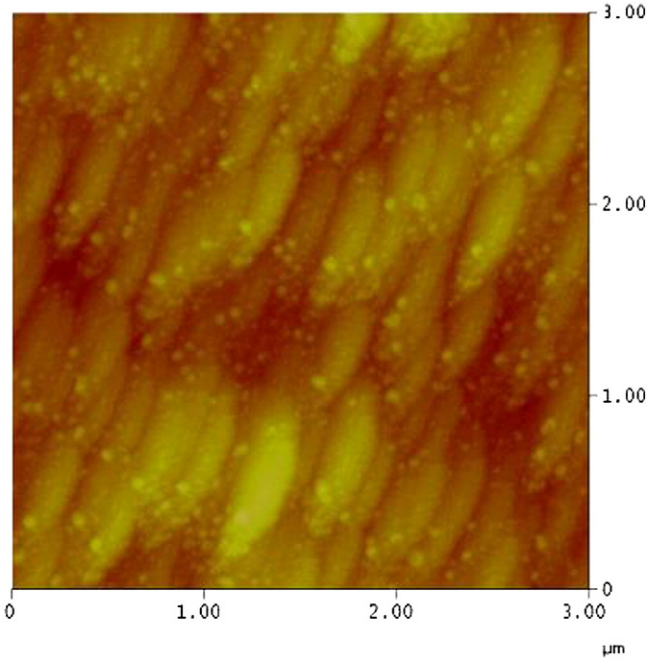

Fig. 7. AFM image of the surface of a Ag–3.14Sn (vol.%) layer sintered for 15 min at 170 °C.

References

[1] M.G. Pecht, A. Govind, In-situ measurements of surface mount IC package deformations during reflow soldering, IEEE Trans. Comp., Packag., Manufact. Technol., 20, 1997, p. 207.
[2] T.Y. Tee, Z. Zhong, Integrated vapor pressure, hygroswelling, and thermo-mechanical stress modeling of QFN package during reflow with interfacial facture mechanics analysis, Microelectron. Reliab. 44 (2004) 105.
[3] S. Zhao, X. Pang, Investigation of delamination control in plastic package, Microelectron. Reliab. 49 (2009) 350.
[4] S.P. Gurrum, S.K. Suman, Y.K. Joshi, A.G. Fedorov, Thermal issues in next-generation integrated circuits, IEEE Trans. Dev. Mater. Reliab. 4 (2004) 709.
[5] R. Singh, A. Akbarzadeh, M. Mochizuki, Sintered porous heat sink for cooling of high-powered microprocessors for server applications, Int. J. Heat Mass Transfer 52 (2009) 2289.
[6] S.K. Kang, A.K. Sarkhel, Lead (Pb)-free solders for electronic packaging, J. Electron. Mater. 23 (1994) 701.
[7] S. Kikuchi, M. Nishimura, K. Suetsugu, T. Ikari, K. Matsushige, Strength of bonding interface in lead-free Sn alloy solders, Mater. Sci. Eng. A 319 (2001) 475.
[8] K. Suganuma, T. Sakai, K. Kim, Y. Takagi, J. Sumimoto, M. Ueshima, Thermal and mechanical stability of soldering QFP with Sn–Bi–Ag lead-free alloy, IEEE Trans. Electron. Packag. Manuf. 25 (2002) 257.
[9] W. Dong, Y. Shi, Z. Xia, Y. Lei, F. Guo, Effects of trace amount of rare earth additions on microstructure and properties of Sn–Bi-based solder alloy, J. Electron. Mater. 37 (2008) 982.
[10] Y. Shiue, T. Chuang, Effect of La addition on the interfacial intermetallics and bonding strengths of Sn–58Bi solder joints with Au/Ni/Cu pads, J. Alloys Compd. 491 (2010) 610.
[11] M. Mccormack, H.S. Chen, G.W. Kammlott, S. Jin, Significantly improved mechanical properties of Bi–Sn solder alloys by Ag-doping, J. Electron. Mater. 26 (1997) 954.
[12] M. Takagi, Electron-diffraction study of liquid–solid transition of thin metal films, J. Phys. Soc. Jpn. 9 (1954) 359.
[13] Y.H. Jo, I. Jung, C.S. Choi, I. Kim, H.M. Lee, Synthesis and characterization of low temperature Sn nanoparticles for the fabrication of highly conductive ink, Nanotechnology 22 (2011) 225701 (8 pp.).
[14] P.-C. Huang, J.-G. Duh, Effects of different surfactant additions and treatments on the characteristics of tin nanosolder by chemical reduction method, Orlando, U.S.A., May, 2008 58th Electronic Components and Technology Conference (ECTC) Proceedings, 2008, p. 431.
[15] H. Jiang, K. Moon, F. Hua, C.P. Wong, Synthesis and thermal and wetting properties of tin/silver alloy nanoparticles for low melting point lead-free solders, Chem. Mater. 19 (2007) 4482.
[16] L.-Y. Hsiao, J.-G. Duh, Revealing the nucleation and growth mechanism of a novel solder developed from Sn–3.5Ag–0.5Cu nanoparticles by a chemical reduction method, J. Electron. Mater. 35 (2006) 1755.
[17] C.Y. Lin, U.S. Mohanty, J.H. Chou, Synthesis and characterization of Sn–3.5Ag–XZn alloy nanoparticles by the chemical reduction method, J. Alloys Compd. 472 (2009) 281.
[18] Y.H. Jo, J.C. Park, J.U. Bang, H. Song, H.M. Lee, New synthesis approach for low temperature bimetallic nanoparticles: size and composition controlled Sn–Cu nanoparticles, J. Nanosci. Nanotechnol. 11 (2011) 1037.
[19] S.L. Lai, J.Y. Guo, V. Petrova, G. Ramanath, L.H. Allen, Size-dependent melting properties of small tin particles: nanocalorimetric measurements, Phys. Rev. Lett. 77 (1996) 99.
[20] H. Jiang, K. Moon, H. Dong, F. Hua, C.P. Wong, Size-dependent melting properties of tin nanoparticles, Chem. Phys. Lett. 429 (2006) 492.
[21] S.-S. Chee, J.-H. Lee, Effects of reductant amount and capping agent on tin nanoparticles synthesis using a tin(II) 2-ethylhexanoate precursor, Adv. Mater. Res. 530 (2012) 52.
[22] S.-S. Chee, J.-H. Lee, Effects of process parameters in synthesizing Sn nanoparticles via chemical reduction, Electron. Mater. Lett. 8 (2012) 53.
[23] F. Fievet, J.P. Lagier, B. Blin, B. Beaudoin, M. Figlarz, Homogeneous and heterogeneous nucleations in the polyol process for the preparation of micron and submicron size metal particles, Solid State Ionics 32 (33) (1989) 198.
[24] S.-S. Chee, J.-H. Lee, Reduction synthesis of tin nanoparticles using various precursors and melting behavior, Electron. Mater. Lett. 8 (2012) 587.
[25] T. Hinotsu, B. Jeyadevan, C.N. Chinnasamy, K. Shinoda, K. Tohji, Size and structure control of magnetic nanoparticles by using a modified polyol process, J. Appl. Phys. 95 (2004) 7477.
[26] V.K. La Mer, R.H. Dinegar, Theory, production and mechanism of formation of monodispersed hydrosols, J. Am. Chem. Soc. 72 (1950) 4847.
[27] V.K. La Mer, Nucleation in phase transitions, Ind. Eng. Chem. 44 (1952) 1270.

[28] B.K. Park, S. Jeong, D. Kim, J. Moon, S. Lim, J.S. Kim, Synthesis and size control of monodisperse copper nanoparticles by polyol method, J. Colloid Interface Sci. 311 (2007) 417.
[29] J.T.G. Overbeek, Monodisperse colloidal systems, fascinating and useful, Adv. Colloid Interface Sci. 15 (1982) 251.
[30] Y. Wang, J.Y. Lee, T.C. Deivaraj, A microemulsion-based preparation of tin/tin oxide core/shell nanoparticles with particle size control, J. Mater. Chem. 14 (2004) 362.
[31] P. Bommersbach, M. Chaker, M. Mohamedi, D. Guay, Physico-chemical and electrochemical properties of platinum–tin nanoparticles synthesized by pulsed laser ablation for ethanol oxidation, J. Phys. Chem. C 112 (2008) 14672.
[32] Md.T. Uddin, Y. Nicolas, C. Olivier, T. Toupance, L. Servant, M.M. Müller, H.-J. Kleebe, J. Ziegler, W. Jaegermann, Inorg. Chem. 51 (2012) 7764.
[33] L. Renard, O. Babot, H. Saadaoui, H. Fuess, J. Brötz, A. Gurlo, E. Arveux, A. Klein, T. Toupance, Nanoscale 4 (2012) 6806.
[34] K.X. Yao, H.C. Zeng, ZnO/PVP nanocomposite spheres with two hemispheres, J. Phys. Chem. C 111 (2007) 13301.
[35] F. Bonet, K. Tekaia-Elhsissen, K.V. Sarathy, Study of interaction of ethylene glycol/PVP phase on noble metal powders prepared by polyol process, Bull. Mater. Sci. 23 (2000) 165.
[36] Y. Zhang, J.Y. Liu, S. Ma, Y.J. Zhang, X. Zhao, X.D. Zhang, Z.D. Zhang, Synthesis of PVP-coated ultra-small Fe_3O_4 nanoparticles as a MRI contrast agent, J. Mater. Sci. Mater. Med. 21 (2010) 1205.
[37] Z. Zhang, B. Zhao, L. Hu, PVP protective mechanism of ultrafine silver powder synthesized by chemical reduction processes, J. Solid State Chem. 121 (1996) 105.
[38] S. Wei, Y. Zhang, M. Zhou, Toluene sensing properties of SnO_2–ZnO hollow nanofibers fabricated from single capillary electrospinning, Solid State Commun. 151 (2011) 895.
[39] S. Jeong, K. Woo, D. Kim, S. Lim, J.S. Kim, H. Shin, Y.N. Xia, J. Moon, Controlling the thickness of the surface oxide layer on Cu nanoparticles for the fabrication of conductive structures by ink-jet printing, Adv. Funct. Mater. 18 (2008) 679.
[40] S.-S. Chee, J.-H. Lee, Synthesis of tin nanoparticles through modified polyol process and effects of centrifuging and drying on nanoparticles, Trans. Nonferrous Met. Soc. China 22 (2012) s707.